Radiation Physics and Chemistry 165 (2019) 108379

Contents lists available at ScienceDirect

Radiation Physics and Chemistry

journal homepage: www.elsevier.com/locate/radphyschem

Observation of radiation enhanced phase formation and subsequent dissolution at very high doses in Ar^{9+} ion irradiated Ti-modified stainless steel

N. Gayathri, Kalipada Das, P. Mukherjee*, Ranjini Menon, P.Y. Nabhiraj

Variable Energy Cyclotron Centre, HBNI, 1/AF Bidhannagar, Kolkata, 700064, India

ARTICLE INFO

Keywords:
Radiation damage
X-ray diffraction
Energy dispersive X-ray analysis

ABSTRACT

Samples of Ti-modified stainless steel alloy have been irradiated using 315 KeV Ar^{9+} ion to varying doses resulting in high dpa levels from 100 to 400. The variation of the secondary phase present in the sample as a function of irradiation dose has been characterised using Grazing Incidence X-ray Diffraction measurements. Energy Dispersive X-ray mapping of the irradiated volume has also been carried out to see the variation in the spatial distribution of the major alloying elements in the un-irradiated and irradiated samples as a function of dose. The study reveals that there is enhancement of secondary phases due to irradiation, which at very high doses re-dissolves into the matrix.

1. Introduction

The 15Cr–15Ni titanium modified stainless steel (Alloy D9) in the 20% cold worked condition is the structural material for fuel pin and wrapper tubes for sodium cooled fast nuclear reactors (Hamilton et al., 1987; Smith, 1984; Kesternich and Rothaut, 1981; Harries, 1978; Ikai et al., 1987). This material has been chosen from the considerations of good combination of high temperature tensile and creep strength properties, irradiation creep resistance and resistance to irradiation induced void swelling (Hamilton et al., 1987; Smith, 1984; Kesternich and Rothaut, 1981; Harries, 1978; Ikai et al., 1987). In general, during irradiation, a significant amount of energy ($\sim 10^8$ J/mol) is deposited by the energetic particles during their successive collisions with the material in the form of defects (Russel, 1984). This energy is then available to cause a variety of microstructural changes including phase transformation which are not observed under thermodynamic condition (Russel, 1984; Motta and Olander, 2017; Martin et al., 1984; Wiedersich et al., 1986). In the absence of irradiation, the thermodynamic parameters act as the driving force for determining the relative stability of phases and thermally-driven kinetics associated with point defect migration determine the rates of phase transformations (Martin et al., 1984). During irradiation, the stability of the phases and the kinetics of phase transformation may be altered depending upon the dose, dose rate, temperature etc. These changes in phase stability have huge consequences for material behaviour under irradiation (Martin et al., 1984). Some of the major effects are pressure vessel embrittlement (by the formation under irradiation of Cu-rich precipitates), irradiation induced sensitization to stress-corrosion cracking (by irradiation induced segregation and precipitation), and irradiation enhanced growth (by precipitate dissolution and nucleation of c-component dislocations) (Martin et al., 1984). The objective of this paper is to determine the effect of irradiation on the segregation due to spatial redistribution of solute atoms and phase stability in advanced austenitic alloy, D9. Several attempts have been made to address the issues of radiation induced segregation on irradiated austenitic stainless steel and D9 using TEM studies and PAS studies (Du et al., 2017; David et al., 2009; Arunkumar et al., 2009). The swelling behaviour of 20% cold-worked 15–15Ti steels with (0.23–0.40) wt% titanium and (0.42–0.81) wt% silicon content after heavy-ion beam irradiation has been investigated by transmission electron microscopy (Du et al., 2017). The void swelling behaviour of (15Ni–14Cr) Ti-modified steels simulated by heavy ion irradiation has been investigated using step height measurements and positron annihilation spectroscopy (David et al., 2009). The performance of 20% cold worked SS316 has been assessed by examining the cladding and wrapper of FBTR at various displacement damages (Karthik et al., 2011). The effect of electron irradiation with energy of 1.0–2.3 MeV on the structure-phase stability of austenitic chromium-nickel and chromium-manganese stainless steels has been studied (Bystrov et al., 1983). Allen et al. have studied the radiation-induced grain boundary segregation, and hardening in a series of Fe-Cr-Ni alloys (Allen et al., 2002) by FEG-STEM and Microhardness. In the present study, an attempt has been made to study the evolution of

* Corresponding author.
E-mail address: paramita@vecc.gov.in (P. Mukherjee).

https://doi.org/10.1016/j.radphyschem.2019.108379
Received 20 April 2018; Received in revised form 28 January 2019; Accepted 22 June 2019
Available online 24 June 2019
0969-806X/

Fig. 1. Optical micrograph of the D9 sample.

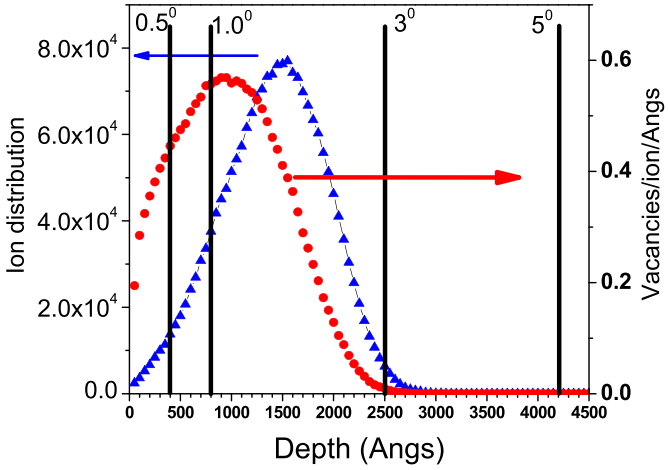

Fig. 2. SRIM results of the Ar ion irradiation in D9 sample. The red curve shows the vacancy distribution and the blue curve shows the Ar ion distribution in the sample. (For interpretation of the references to color in this figure legend, the reader is referred to the Web version of this article.)

irradiation enhanced phase in D9 alloy by Grazing incidence X-ray diffraction (GIXRD) and radiation induced segregation by Energy Dispersive X-ray analyser (EDAX) attached with FEG-SEM. X-ray line profile analysis of the GIXRD data has also been carried out to understand the changes in the microstructural parameters (represented by the domain size and the associated microstrain within the domain).

2. Experimental techniques

The D9 sample used for this study was obtained in the form of rods of 30 mm diameter in the hot rolled condition. The composition of D9 is C: 0.045, Cr: 13.88, Ni: 15.24, Mo: 2.12, Ti: 0.23, B: 12 ppm, Mn: 2.12, Si: 0.64, Cu: 0.017, As: 0.0019, N: 0.0021, Al: 0.01, Co: 0.007, S: < 0.005, P: < 0.005, Nb: < 0.005, V: < 0.01, Ta: < 0.01, Fe: Rest. Rods of 26 mm diameter were machined from these hot rolled rods and given a solution annealing treatment at 1373 K for 1/2 h followed by water quenching. 10 mm × 10 mm size samples were machined from these rods for the irradiation study. The samples were mechanically polished using 1 μm diamond paste before carrying out the irradiation. Fig. 1 shows the optical micrograph of annealed D9 alloy with a grain size around 50 μm.

The D9 samples were irradiated using 315 KeV Ar^{9+} from 6.45 GHz Electron Cyclotron Resonance (ECR) ion source at Variable Energy Cyclotron Centre, Kolkata, India. A set of 4 samples were irradiated at a constant current of 1pμA (~6.25×10^{12} ions/cm^2/sec) under vacuum (pressure ~10^{-6} mbar) using Ar^{9+} to get the total doses of 4.7×10^{16}, 9.4×10^{16}, 1.4×10^{17} and 1.9×10^{17} Ar^{9+}/cm^2. Fig. 2 shows the range of Ar^{9+} ions and the damage profile within the D9 sample calculated using the SRIM-2013 (Ziegler, 2015) software. The displacements per atom (dpa) was calculated and found to be around 100, 200, 300 and 400 dpa respectively for the doses mentioned above.

2.1. GIXRD measurements

The unirradiated and irradiated samples were characterised using GIXRD at different angles of incidence to cover the entire damage depth. The experiment was carried out using parallel beam optics mode of Bruker D8-Advance Diffractometer. The diffracted beam was collected using a LYNX EYE detector in the 0D mode. The data was taken at an interval of 0.02 deg with an averaging time of 15 s/step. The high fluorescence background generally observed in Fe based samples due to Cu Kα radiation was avoided by selecting the detector discriminator levels appropriately. In order to study the damage region as a function of the depth, the GIXRD measurements were performed at four different incident angles namely 0.5^0, 1^0, 3^0 and 5^0. The angles were chosen so as to cover the different damage region as shown in Fig. 2. The patterns obtained at different angles will provide microstructural information from different layers within the samples. The linear absorption coefficient (μ) of Fe for CuK_α-X-ray is 2411 cm^{-1}. The depth of penetration of CuK_α calculated using eqn. (1) is about 360 Å, 725 Å, 2170 Å and 3610 Å respectively at different incident angles and is marked by the vertical bars in Fig. 2.

$$\tau = \frac{\sin \alpha}{\mu} \tag{1}$$

For the analysis of the data to obtain the microstructural parameters, the instrumental broadening correction was performed using a standard defect free LaB_6 sample at the same angles of incidence and the instrumental parameters were obtained from the Caglioti plot (Caglioti et al., 1958).

2.2. EDX study

Elemental mapping of the Ni and Cr in the unirradiated and irradiated samples were carried out using the Energy Dispersive X-ray (EDX) measurements using the X-Max^N Silicon Drift Detector of size 20 mm^2 from Oxford instruments fitted to an FE-SEM Supra 55™ (Make:Carl Zeiss). In order to obtain information only from the irradiated depth of the sample (2500 Å), the electron beam energy has been optimized using Castaing's relation (Castaing and Marion, 1960). Accordingly, the EDX mapping was carried out using 12 KeV electron beam. An area of 200 μm × 200 μm has been scanned and the elemental analysis has been carried out for the two major alloying elements Ni and Cr.

3. Method of analysis X-ray line profile analysis - modified Rietveld method using Maud

This modified Rietveld method is a whole pattern fitting technique (implemented in the program MAUD (Lutterotti et al., 1999a; Lutterotti et al., 1999b)). The microstructural parameters (such as domain size, microstrain, planar faults etc.) are introduced as fitting parameters in the program (Lutterotti et al., 1992, 1999a, 1999b; Lutterotti and Scardi, 1990). The methodology used in the program is briefed below:

The profile of X-ray pattern at any diffraction angle (2θ) is represented as the convolution of B the true line broadening related to the sample, I_S the symmetric part of the instrumental broadening function and I_a the asymmetric instrumental function (Lutterotti and Scardi, 1990).

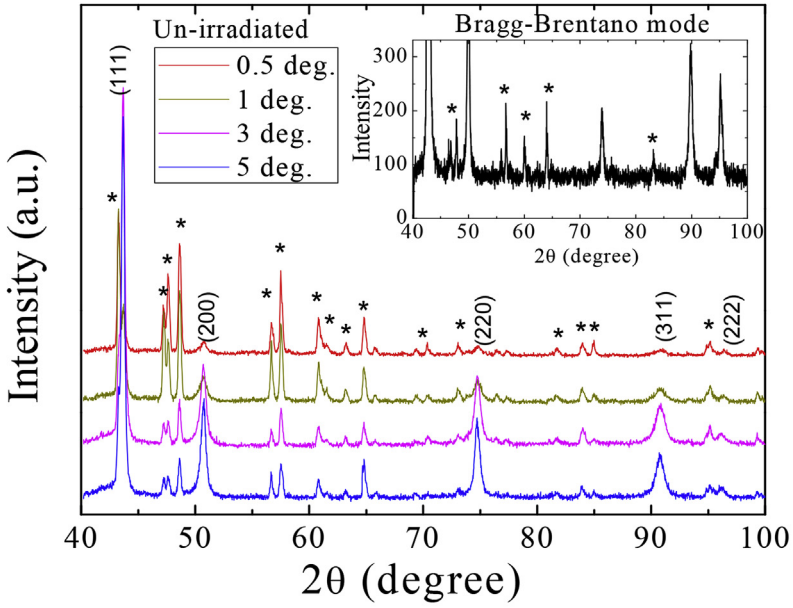

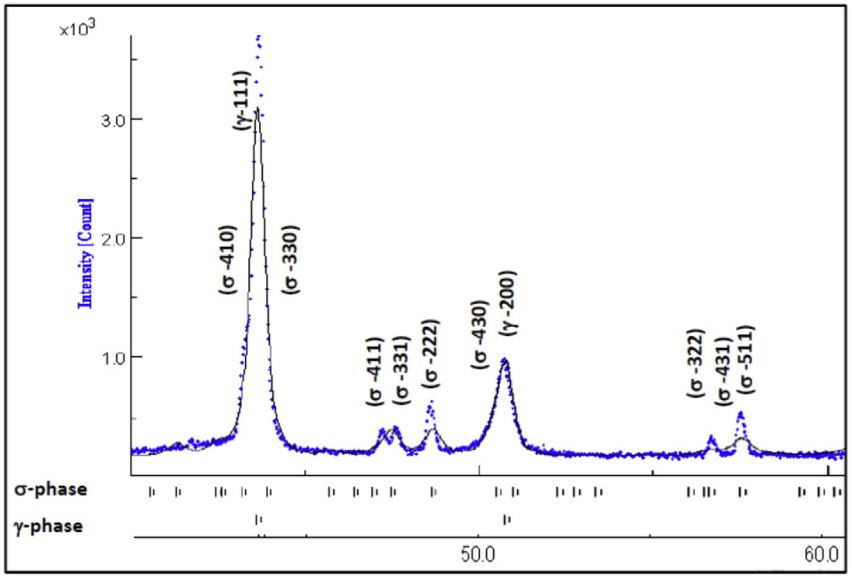

Fig. 3. a: GIXRD pattern obtained from the unirradiated sample at different angles of incidence. Inset shows the XRD pattern of the same sample taken in the Bragg-Brentano (θ-θ) geometry mode. b: Diffraction pattern of un-irradiated D9 sample for 1° incident angle. The peaks are indexed for the γ phase and the σ phase.

$$Y_C(2\theta) = [B * (I_S * I_a)](2\theta) + bkg$$

Here both B and I_S are represented by a pseudo-Voigt (pV) function and the procedure described by de Keijer et al. (de Keijser ThHLangford et al., 1982) is used to convolute them. The result is then numerically convoluted with I_a (represented by an exponential function) (Lutterotti and Scardi, 1990). The explicit form of the pV function can be written as (Lutterotti and Scardi, 1990)

$$pV(2\theta) = \sum_{\alpha_1\alpha_2} I_{nt}[(1-\eta)(1+S^2)^{-1} + \eta \exp(-ln2 \times S^2)] \quad (3)$$

$$S = (2\theta - 2\theta_0)/HWHM$$

where HWHM and η are the shape parameters. The pV function for the true line broadening B (in the sample) is related to the coherent domain size (D), and the r.m.s. microstrain ($< ??^2 >^{1/2}$) (assuming a Gaussian strain distribution) as shown below (Lutterotti and Scardi, 1990; Nandi et al., 1984)

$$Z/(Z+1)\exp[-(Z+1)^2/(16\ln 2)] + 1/(Z+1)\exp[-(Z+1)/2] = \exp\left[-\pi^2 < \varepsilon^2 > \frac{D^2}{(2d^2)} - 1/2\right]$$

$$HWHM = \arcsin[\lambda(Z+1)/(4\pi D) + \sin\theta_0] - \theta$$

$$\eta = Z/[Z + (\pi/\ln 2)^{1/2}]$$

Hence, knowing D and $< \varepsilon^2 >$ one can obtain the shape parameters HWHM and η related to the microstructural broadening and hence perform the fitting of the data by the Rietveld method.

The procedure similar to that described by Wenk et al. (2003) has been followed. Initially, the XRD data are refined taking into account the instrumental parameters, the background and the crystallographic parameters (lattice parameters of parent phase and segregated phases). This is then followed by the introducing the microstructural parameters (relative isotropic crystallite size (Ds) and r.m.s. microstrain $< \varepsilon_L^2 >^{1/2}$ as the fitting parameters in the refinement (Wenk et al., 2003).

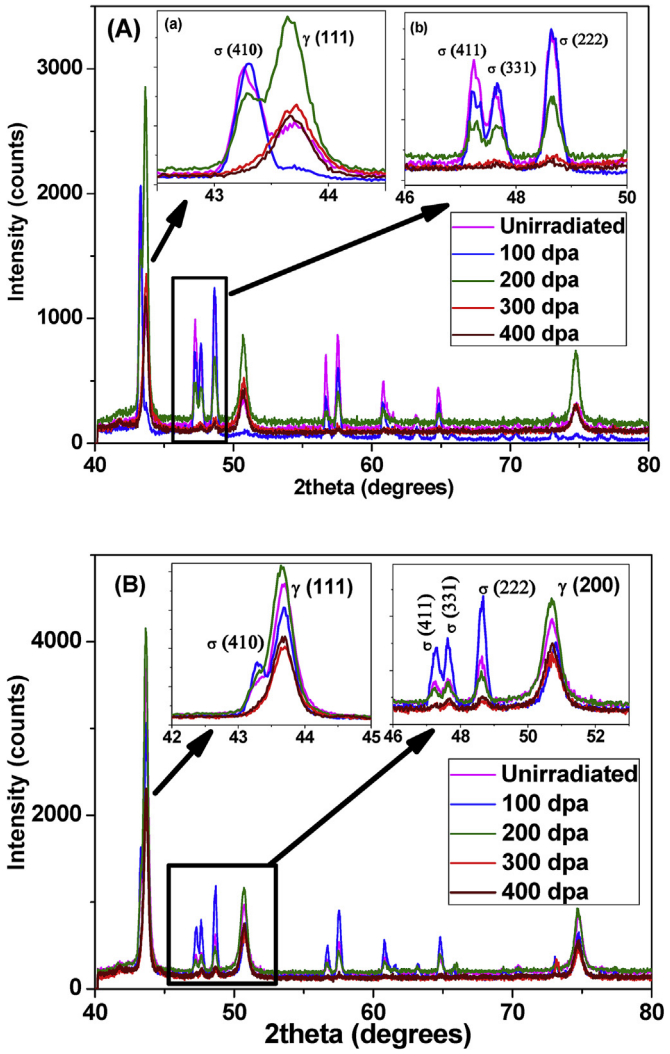

Fig. 4. (A) and (B) represents the diffraction patterns for 1° and 3° incident angles respectively. Insets show the expanded region of the X-ray pattern.

4. Results and discussion

Fig. 3a represents the GIXRD pattern of the un-irradiated D9 sample at different incident angles. It can be seen from Fig. 3a that in addition to the γ (fcc) phase of the D9 sample, some additional peaks are observed (marked as *). The d-spacing of most of these lines matches with the σ phase observed in stainless steel samples (Hsieh and Wu, 2012; Villanueva et al., 2006). The diffraction peaks for the γ phases and σ phase have been indexed in Fig. 3b. It is clearly seen that the additional phases present within the γ matrix vary from the surface along the depth. The peak intensities of the σ phase are found to be more for incident angles 0.5 and 1° as compared to incident angle 3 and 5° (at the matrix). The inset of Fig. 3a shows the X-ray pattern of the un-irradiated sample obtained using the Bragg-Brentano geometry. This indicates that the σ phase is present even in the bulk of the sample (at least up to 2 μm which is the average depth of penetration of the Cu Kα X-ray in the Bragg-Brentano mode).

In this present study we have carried out the mixed phase analysis of experimental data (both unirradiated and irradiated samples) by using MAUD software considering the γ iron and the σ phase as reported earlier (Hsieh and Wu, 2012; Villanueva et al., 2006). Similar studies using GIXRD have been carried out on the samples irradiated at 100 dpa, 200dpa, 300 dpa and 400dpa. Fig. 4 represents the XRD pattern of unirradiated and irradiated samples at grazing angle 1° and 3°. By indexing the pattern, it was found that the highest intensity peak (111) of γ phase overlaps with (410) peak of σ phase. It is seen from Fig. 4a (grazing incidence angle 1° corresponding to 725 Å) that at 100 dpa, the intensity of (111) and (200) peaks of the γ phase did not change significantly as compared to the un-irradiated sample. On increasing the dose to 200 dpa, the intensity of this peak drastically increases. At higher dpa (300 dpa and 400 dpa), clearly there is a broadening of these peaks with reduced intensity. On the contrary, the intensity of the (331) and (411) peak of the σ phase decreases at 300 and 400dpa.

Recently, M. Frelek-Kozak et al. (Kurpaska et al., 2018) have reported the results of GIXRD measurements on low energy ion irradiated ODS RAF steels. The irradiation was carried out using sequential and dual beam low energy ions (30 keV He and 150 keV Fe). They observed peak shift in the XRD pattern of the irradiated samples as a function of dpa and attributed the shift to be due to internal stresses developed in the material due to ion irradiation. It has to be noted that significant peak shift is observed in the He ion irradiated samples (sequential and dual beam) as compared to the samples which have been irradiated by only Fe ion. They have also clearly mentioned in their manuscript that, the observation may be treated as a tendency and more accurate experiments and analysis is needed to be carried out. Our irradiation experiments were carried out using 315 keV Ar ion which has a penetration depth of about 2500 Å. We have carried out GIXRD measurements on the irradiated samples at various incident angles covering the full depth of the ion irradiation. Our results did not reveal any peak shift in the XRD pattern as a function of dose. This can be seen in Fig. 4A and B of the manuscript where the XRD patterns obtained at 1° and 3° incident angles are shown.

Extensive studies have been done on the phase transition during irradiation in austenitic steels (Pechenkin and Epov, 1993; Jiao and Was, 2011; Gary, 2016), still there is no established trend that predicts the direction of irradiation-induced phase changes. During irradiation, redistribution of alloying elements occurs which causes either dissolution of precipitates or formation of irradiation induced precipitates. These phase transition (i.e. dissolution or formation) depends upon the irradiation condition, materials composition and initial microstructure (Gary, 2016). Irradiation can alter phase transformations simply by accelerating the phase transformation kinetics, through radiation-enhanced diffusion (Gary, 2016; Sizmann, 1978). Here, we find that the intensity of γ phase in D9 alloy did not alter at 100 dpa, though there is a clear indication of increase in intensity of σ phase due to radiation enhanced phase transformation of σ phase. At higher dpa, the dislodgement of atoms from the σ phase makes the phase unstable causing dissolution of σ phase for which the intensity of (331) and (411) of σ phase decreases. As a result, the intensity of (111) which denotes the matrix phase increases. In Fig. 4b, (at incidence angle 3° corresponding to 2170 A), almost the entire irradiated area is covered as shown in Fig. 2. Similar observations are also made from Fig. 4b as seen in Fig. 4a. Here the peak intensity of the matrix phases did not change up to 100dpa, though the intensity of (331) and (411) of σ phase has increased at 100dpa indicating the radiation enhanced phase transformation. At higher dpa, dissolution of σ phase occurs due to redistribution of alloying elements.

Fig. 5a shows the phase percentage of the γ and the σ phases obtained from the XRD analysis. It is to be noted that the phase analysis has been carried out by considering the presence of only the two major phases (γ and σ phases). It can be seen that the σ phase content increases at 100 dpa and then shows a decrease with further irradiation dose. Fig. 5b shows the microstructural parameters domain size and microstrain of the two phases. It can be noted that the domain size of the γ phase is lower than that of the σ phase. At 100 and 200 dpa, the domain size of the σ phase increases comparatively and then decreases with further increase in dose (300 and 400 dpa). There is no significant change in the domain size of the γ phase. Although, the microstrain values of the γ phase are slightly higher compared to that of the σ phase there is no significant or systematic variation with dose.

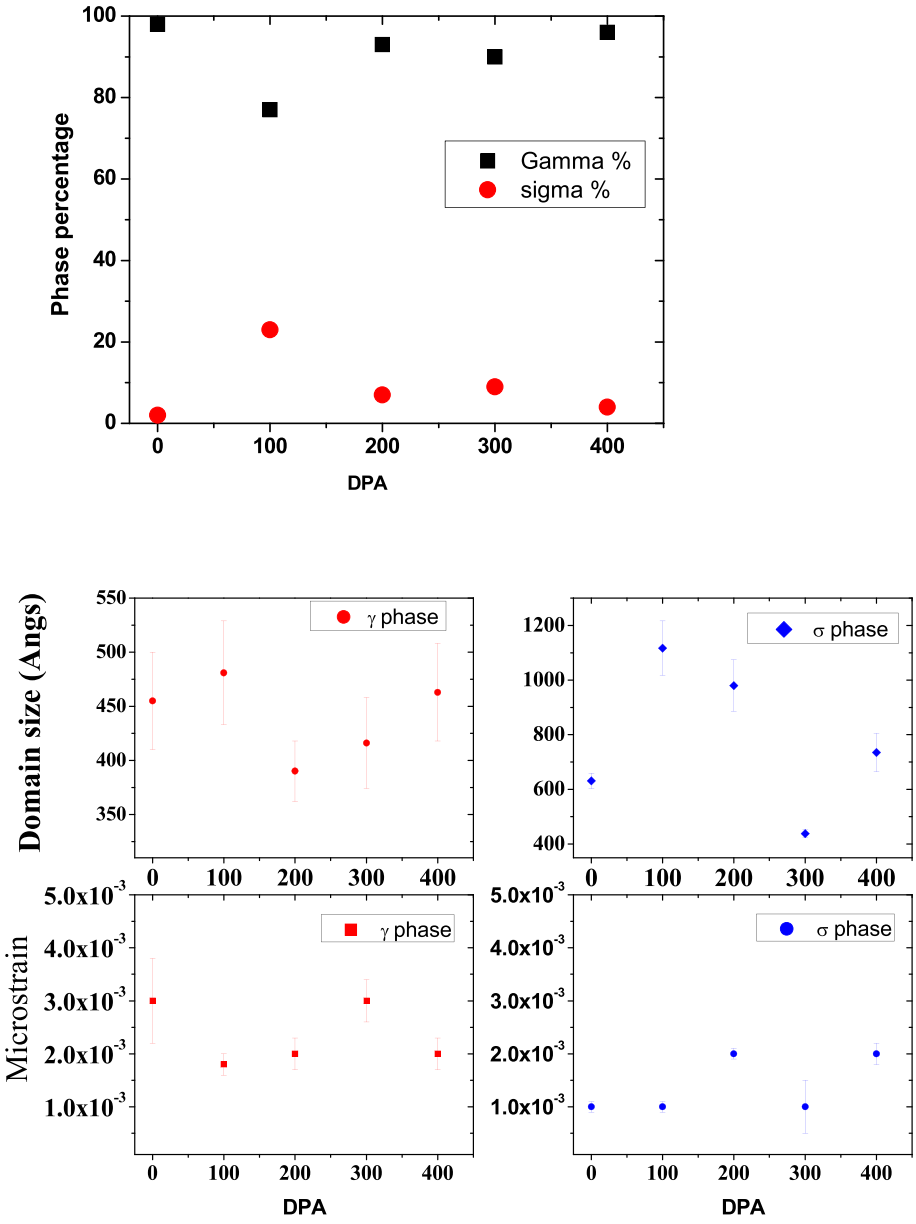

Fig. 5. a. Phase percentage of the γ and σ phase obtained from the MAUD analysis carried out from GIXRD data collected at incident angle of 3 degs. b: Microstructural parameters of the γ phase and the σ phase obtained from the MAUD analysis carried out from GIXRD data collected at incident angle of 3 degs.

The redistribution of major alloying elements like Ni and Cr as a function of dpa has been studied by Energy Dispersive X-ray Spectroscopy (EDX) measurements. In case of EDX measurements, we have measured the percentage of the alloying elements present in the samples in several positions (in 8 × 8 matrix as indicated in Fig. 6A) within the sample (~200 μm × ~200 μm). Fig. 6B–(G) shows the contour map of the spatially variation of Cr (red) and Ni (blue) for un-irradiated and the irradiated samples obtained from the 200 μm × 200 μm scan.

It can be clearly seen from Fig. 6B that the un-irradiated sample has a more or less uniform distribution of the major alloying elements Cr and Ni. With irradiation, the special variation of the Cr and Ni increases with the dose as can be seen from Fig. 6(C-E). At the final dose of irradiation ie., 400 dpa (Fig. 6F), the fluctuation of elements decreases, resulting in a more uniform distribution similar to that of the un-irradiated sample. Fig. 7 shows the histogram of the distribution of alloying elements 'Cr' (A) and 'Ni' (B) derived from the 3D contour map. It is clear that the width of the histogram increases upon irradiation showing the spread in the spatial distribution of the Cr and Ni content. However at the highest dose of irradiation, the histogram width decreases indicating the homogenous distribution of the major alloying elements Ni and Cr in the sample. The results obtained from the EDX measurements corroborate well with the GIXRD measurements in the sample.

5. Conclusion

The irradiation enhanced phase formation and its dissolution in D9 alloy have been studied by GIXRD and EDX measurements. GIXRD studies as a function of depth of the damage region clearly indicates the enhancement and dissolution of σ phase in the γ matrix as a function of dose. EDX studies of the rich alloying elements like Ni and Cr in the D9 alloy also give a clear signature of their distribution in the matrix with dose of irradiation. It was found at higher doses, the distribution of the alloying elements matches with those of the unirradiated sample indicating the dissolution of the irradiation enhanced phases into the

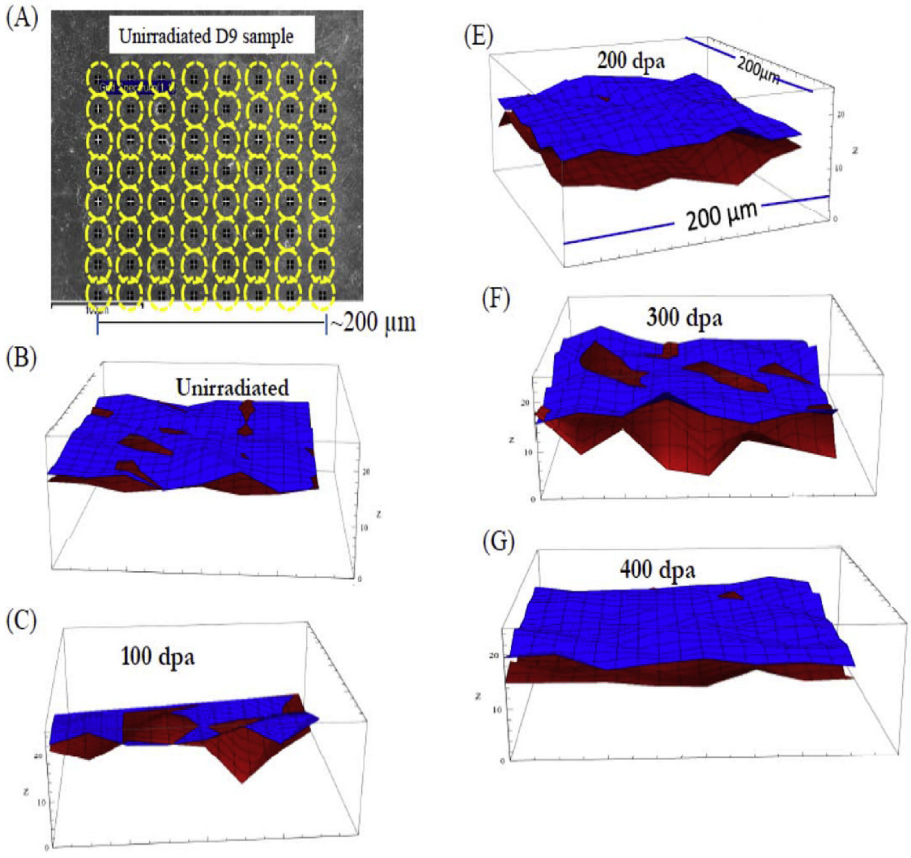

Fig. 6. (A) Representative Scanning Electron Microscopy (SEM) image of D9 un-irradiated sample selected for Energy Dispersive X-ray Spectroscopy (EDS) study The yellow circles show the area from which the information is collected. 8 × 8 matrix scan covered an area of 200 μmx200 μm. (B)–(G) represents the spatially variation of Cr (red color) and Ni (blue color) for un-irradiated and the irradiated samples. (For interpretation of the references to color in this figure legend, the reader is referred to the Web version of this article.)

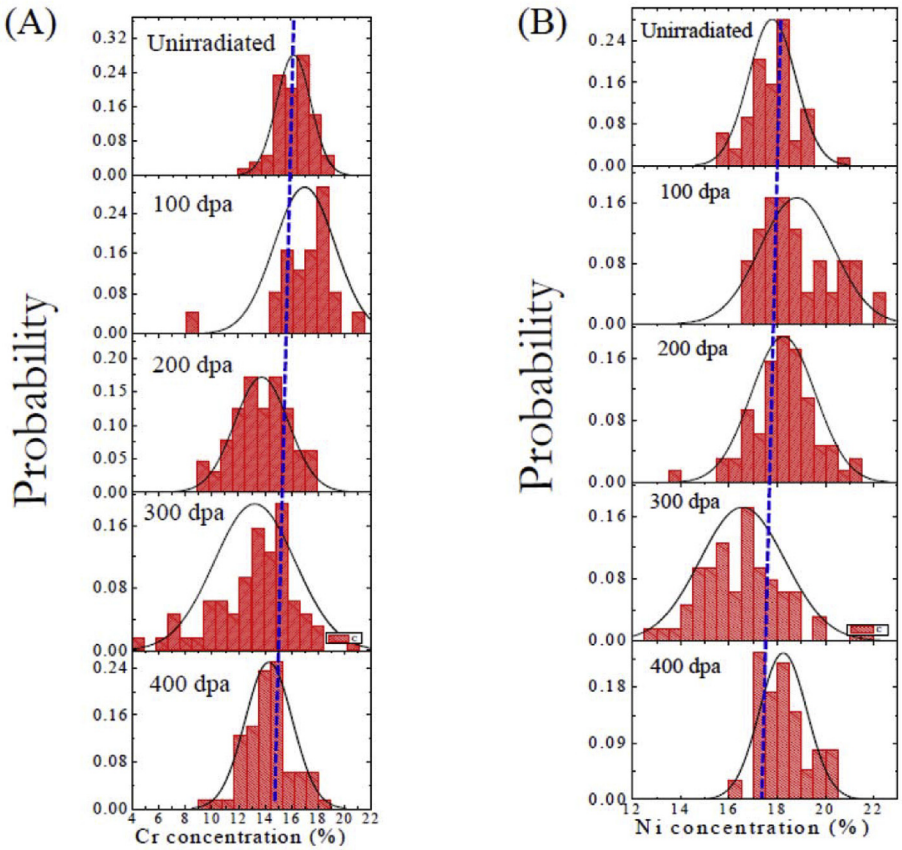

Fig. 7. The statistics of the spatial variation of (A) Cr and (B) Ni for un-irradiated and irradiated D9 samples.

matrix.

References

Allen, T.R., Cole, J.I., Was, G.S., Kenik, E.A., 2002. In: Presented at National Society of Black Physicists Conference Proceedings Huntsville Alabama March 13 – 16, . https://digital.library.unt.edu/ark:/67531/metadc733545/.

Arunkumar, J., Abhaya, S., Rajaraman, R., Amarendra, G., Nair, K.G.M., Sundar, C.S., Raj, Baldev, 2009. Phys. Status Solidi C 6, 2319.

Bystrov, L.N., Ivanov, L.I., Ustinovschikov, V.M., 1983. Radiat. Eff. Defect Solid 79, 63.

Caglioti, G., Paoletti, A., Ricci, F.P., 1958. Nucl. Instrum. Methods 3, 223.

Castaing, R., 1960. In: In: Marion, L. (Ed.), Advances in Electronics and Electron Physics, vol. 13. Academic Press, New York, pp. 317.

David, C., Panigrahi, B.K., Amarendra, G., Abhaya, S., Balaji, S., Balamurugan, A.K., Nair, K.G.M., Viswanathan, B., Sundar, C.S., Raj, Baldev, 2009. Surf. Coating. Technol. 203, 2363.

de Keijser ThH, Langford, J.I., Mittmeijer, E.J., Vogels, A.B.P., 1982. J. Appl. Crystallogr. 15, 308.

Du, Ai-Bing, Feng, Wei, Ma, Hai-Liang, Liang, Tian, Yuan, Da-Qing, Fan, Ping, Zhang, Qiao-Li, Huang, Chen, 2017. Acta Metall. Sin. 30, 1049.

Gary, S., 2016. Was, Fundamentals of Radiation Materials Science: Metals and Alloys, second ed. Springer.

Hamilton, M.L., Huang, F.H., Yang, W.J.S., Garner, F.A., 1987. In: Garner, F.A., Igata, N., Henager Jr.C.H. (Eds.), Proceedings of Effects of Radiation on Materials: Thirteenth International Symposium (Part II) Influence of Radiation on Material Properties. American Society for Testing and Materials, ASTM STP 956, Philadelphia, PA, pp. 245–270.

Harries, D.R., 1978. Nucl. Energy 17, 301.

Hsieh, Chih-Chun, Wu, Weite, 2012. ISRN Metallurgy. Article ID 732471 (2011).

Ikai, T., Yuhara, S., Shibara, I., Kubota, H., Itoh, M., Nomura, S., 1987. In: Proceeding of the International Conference on Materials for Nuclear Reactor Core Applications. BNES, London, pp. 203.

Jiao, Z., Was, G.S., 2011. Acta Mater. 59, 1220.

Karthik, V., Murugan, S., Parameswaran, P., Venkiteswaran, C.N., Gopal, K.A., Muralidharan, N.G., Saroja, S., Kasiviswanathan, K.V., 2011. Energy Procedia 7, 257.

Kesternich, W., Rothaut, J., 1981. J. Nucl. Mater. 104, 845.

Kurpaska, M. Frelek-Kozak L., Lesniak, M., Jozwik, I., Jagielski, J., 2018. Fusion Eng. Des. 127, 54–59.

Lutterotti, L., Scardi, P., 1990. Simultaneous structure and size-strain refinement by the Rietveld method. J. Appl. Crystallogr. 23, 246–252.

Lutterotti, L., Scardi, P., Maistrelli, P., 1992. J. Appl. Crystallogr. 25, 459–462.

Lutterotti, L., Matthies, S., Wenk, H.R., 1999a. IUCr: Newsletter of the CPD.

Lutterotti, L., Matthies, S., Wenk, H.-R., 1999b. In: Proceeding of the Twelfth International Conference on Textures of Materials (ICOTOM-12), vol. 1. pp. 1599.

Martin, G., Barbu, 1984. In: Haasen, P., Gerold, V., Wagner, R., Ashby, M.F. (Eds.), Decomposition of alloys: the early Stages,Proceedings of the 2nd Acta-Scripta Metallurgica Conference 1984. Permagon Press, pp. 70–76.

Motta, Arthur T., Olander, Donald R., 2017. Light Water Reactor Materials, vol. I Fundamentals, American Nuclear Society.

Nandi, R.K., Kuo, H.K., Schlosberg, W., Wissler, G., Cohen, J.B., Crist Jr., B., 1984. J. Appl. Crystallogr. 17, 22.

Pechenkin, V.A., Epov, G.A., 1993. J. Nucl. Mater. 207, 303.

Russel, K.C., 1984. Prog. Mater. Sci. 28, 229–434.

Sizmann, R., 1978. J. Nucl. Mater. 69–70, 386.

Smith, D.L., 1984. J. Nucl. Mater. 122, 51.

Villanueva, D.M.E., Junior, F.C.P., Plaut, R.L., Padilha, A.F., 2006. Mater. Sci. Technol. 22, 1098.

Wenk, H.-R., Lutterotti, L., Vogel, S.C., 2003. Nucl. Instrum. Methods A 515, 575.

Wiedersich, H., 1986. Phase stability and solute segregation during irradiation. In: Johnson, R.-A., Orlov, A.N. (Eds.), Physics of Radiation Effects in Crystals. Elsevier Science Publishers B.V..

Ziegler, J., 2015. SRIM – the Stopping and Range of Ions in Matter, fifteenth ed. .